Scaling of thin wire cylindrical compression with material, diameter, and laser energy after 100 fs Joule surface heating

L. Yang ✉ 📧 ; M.-L. Herbert 📧 ; C. Baehtz; V. Bouffetier 📧 ; E. Brambrink 📧 ; T. Dornheim 📧 ; N. Fefeu;
T. Gawne 📧 ; S. Goede; J. Hagemann 📧 ; H. Höppner 📧 ; L. G. Huang ✉ 📧 ; O. Humphries 📧 ; T. Kluge 📧 ;
D. Kraus 📧 ; J. Lütgert 📧 ; J.-P. Naedler 📧 ; M. Nakatsutsumi 📧 ; A. Pelka 📧 ; T. R. Preston 📧 ; C. B. Qu 📧 ;
S. V. Rahul 📧 ; L. Randolph 📧 ; R. Redmer 📧 ; M. Rehwald 📧 ; J. J. Santos 📧 ; M. Šmíd 📧 ; U. Schramm 📧 ;
J.-P. Schwinkendorf 📧 ; M. Vescovi ; U. Zastrau ; K. Zeil 📧 ; A. Laso Garcia ✉ 📧 ; T. Toncian 📧 ;
T. E. Cowan 📧

Check for updates

View Online   Export Citation

Articles You May Be Interested In

Dynamic convergent shock compression initiated by return current in high-intensity laser–solid interactions

Matter Radiat. Extremes (June 2024)

High-energy-density plasma in femtosecond-laser-irradiated nanowire-array targets for nuclear reactions

Matter Radiat. Extremes (November 2022)

Thermoreflectance microscopy measurements of the Joule heating characteristics of high- T c superconducting terahertz emitters

J. Appl. Phys. (December 2017)

Scaling of thin wire cylindrical compression with material, diameter, and laser energy after 100 fs Joule surface heating

L. Yang, [1,2,a] M.-L. Herbert, [1,3] C. Baehtz,[1] V. Bouffetier,[1] E. Brambrink,[4] T. Dornheim,[1,5] N. Fefeu,[6] T. Gawne,[1,5] S. Goede,[4] J. Hagemann,[7] H. Höppner,[1] L. G. Huang,[1,a] O. Humphries,[4] T. Kluge,[1] D. Kraus,[1,3] J. Lütgert,[3] J.-P. Naedler,[3] M. Nakatsutsumi,[4] A. Pelka,[1] T. R. Preston,[4] C. B. Qu,[3] S. V. Rahul,[4] L. Randolph,[4] R. Redmer,[3] M. Rehwald,[1] J. J. Santos,[6] M. Šmíd,[1] U. Schramm,[1,2] J.-P. Schwinkendorf,[1,4] M. Vescovi,[1] U. Zastrau,[4] K. Zeil,[1] A. Laso Garcia,[1,a] T. Toncian,[1] and T. E. Cowan[1,2]

AFFILIATIONS

[1] Helmholtz-Zentrum Dresden–Rossendorf, Bautzner Landstraße 400, 01328 Dresden, Germany
[2] Technische Universität Dresden, 01062 Dresden, Germany
[3] Universität Rostock, Institut für Physik, D-18059 Rostock, Germany
[4] European XFEL, Holzkoppel 4, 22869 Schenfeld, Germany
[5] Center for Advanced Systems Understanding (CASUS), D-02826 Görlitz, Germany
[6] Centre Lasers Intenses et Applications (CELIA), Université de Bordeaux-CNRS-CEA, UMR 5107, F-33405 Talence, France
[7] DESY Deutsches Elektronen-Synchrotron, Photon Science, Notkestrasse 85, 22607 Hamburg, Germany

[a] Authors to whom correspondence should be addressed: yanglong@hzdr.de; lingen.huang@hzdr.de; and a.garcia@hzdr.de

ABSTRACT

We present the first systematic experimental validation of return-current-driven cylindrical implosion scaling in micrometer-sized Cu and Al wires irradiated by J-class femtosecond laser pulses. Employing XFEL-based imaging with sub-micrometer spatial and femtosecond temporal resolution, supported by hydrodynamic and particle-in-cell simulations, we reveal how return current density depends precisely on wire diameter, material properties, and incident laser energy. We identify deviations from simple theoretical predictions due to geometrically influenced electron escape dynamics. These results refine and confirm the scaling laws essential for predictive modeling in high-energy-density physics and inertial fusion research.

I. INTRODUCTION

Achieving controlled fusion energy in the laboratory remains one of the most profound challenges in modern physics. At the heart of inertial confinement fusion (ICF) research lies the quest to compress hydrogenic fuel to extreme densities and temperatures, a regime recently accessed by large-scale, multi-kilojoule, and nanosecond-pulse laser facilities such as the National Ignition Facility (NIF) and OMEGA.[1–3] These flagship experiments have, for the first time, demonstrated net energy gain and enabled exploration of matter at multi-gigabar pressures. However, the high cost, low

repetition rate, and diagnostic limitations of such facilities impede systematic investigation of the complex, transient plasma dynamics underlying heating, compression, and instability growth.[4–7] Conventional optical and X-ray backlighting techniques are challenged by the high opacity and ultrafast evolution of the compressed plasma core, leaving important questions unresolved regarding energy coupling, hydrodynamic instability, and material response at relevant pressure, spatial, and temporal scales.[4–8]

Recent studies have shown that short-pulse lasers operating at the J scale can induce micrometer-scale cylindrical implosions, achieving pressures approaching 1 Gbar at stagnation based on

05 February 2026 10:38:38

the hydrodynamic simulation predictions.[9,10] These implosions, driven by surface ablation initiated by hot-electron-induced return currents, provide a highly controllable platform for investigating fundamental high-energy-density (HED) plasma processes. When combined with femtosecond hard X-ray free-electron laser (XFEL) diagnostics, these experiments enable unprecedented temporal (femtosecond) and spatial (sub-micrometer) resolution, directly revealing processes previously inaccessible or unclear, such as instability growth and decay,[11] hole-boring dynamics in wire targets,[12] and laser-driven fast electron transport in solid-density matter.[13,14] Such capability opens new windows into fundamental questions of implosion dynamics and equation-of-state behavior at extremely high pressures.

The physical mechanism driving such implosions involves surface-bound return currents triggered by laser-accelerated hot electrons. When an intense femtosecond laser irradiates a solid target, electrons with energy exceeding MeV are expelled and leave behind a net positive charge;[15–17] rapid neutralization by return currents flowing along the target surface[18–22] can, under the right conditions, drive compressive or pinching forces in wire-like geometries. Indirect evidence of this process was first observed in solid hydrogen-jet targets via optical shadowgraphy probing on the DRACO laser.[10,23] Most notably, the Europe XFEL diagnostics have recently enabled the first direct observation of cylindrical implosions in micrometer-sized metallic wires.[9] While the proof-of-principle study demonstrates the promise of combining femtosecond lasers with XFEL diagnostics for a new path to the highest pressures relevant to ICF research, it remains limited to a single-case demonstration.

A systematic understanding of return-current implosion requires quantitative validation of the underlying scaling laws—specifically, how the peak surface current density j depends on (i) wire radius r, (ii) atomic number Z, and (iii) incident laser energy E_L. Theoretically, return-current models predict an inverse-radius scaling $j \propto r^{-1}$ with only weak material dependence, modified by hot-electron escape dynamics and surface-wave attenuation.[10] Experimental confirmation of these predictions across a broad parameter space is essential both for refining our physical models and for guiding the design of next-generation relativistic femtosecond-laser implosion experiments.

In this work, we present the first experimental validation of return-current scaling in micrometer-sized Cu and Al wires. By combining XFEL-backlit imaging (with sub-micrometer spatial and femtosecond temporal resolution) with hydrodynamic and particle-in-cell (PIC) simulations, we quantify j over a range of wire diameters (10–25 μm), materials (Cu vs Al), and laser energies (0.1–1.35 J). We show that j indeed scales inversely with r, exhibits minimal Z dependence, and follows the predicted $E_L^{2/3}$ law, with systematic deviations of 3% captured by geometry- and attenuation-based correction factors. Our results not only bridge critical gaps between theory and observation, but also establish the scaling behavior of return-current-induced implosions and demonstrate the predictive
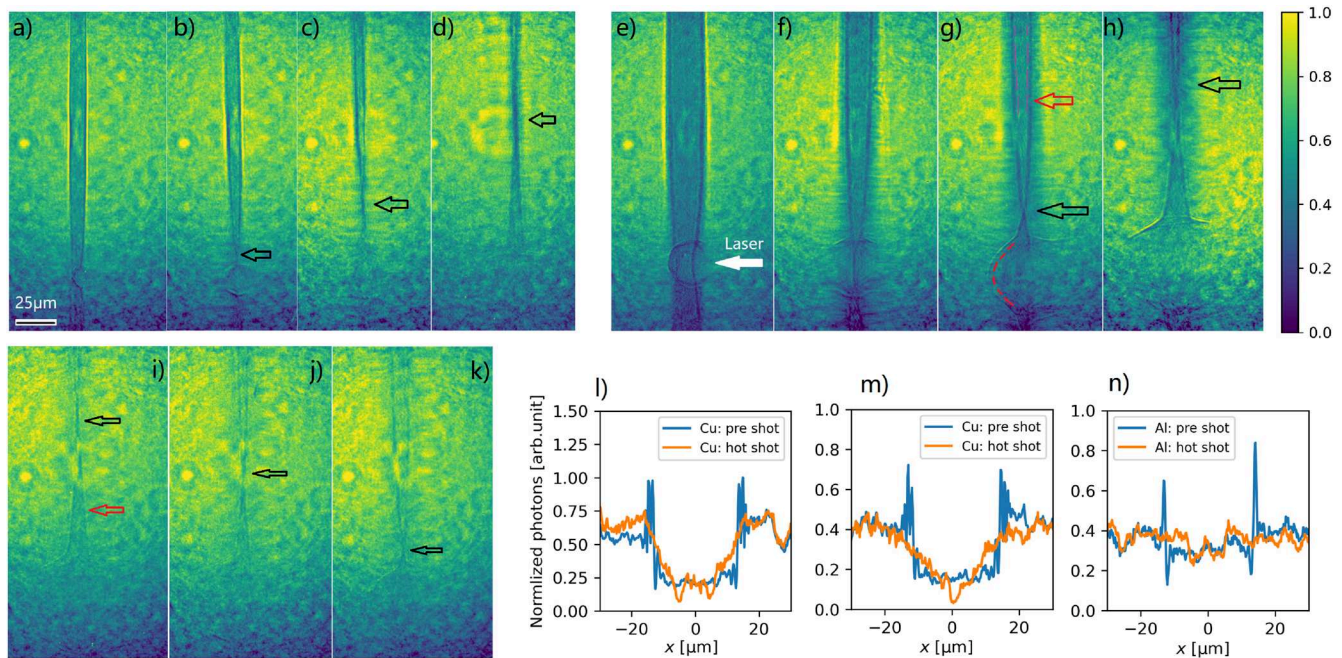
FIG. 1. X-ray images of wire implosions at different time delays. (a)–(d) A 10 μm diameter copper wire at delays of 40, 100, 200, and 250 ps, respectively, after the ReLaX laser. (e)–(h) A 25 μm diameter copper wire at delays of 250, 500, 700, and 1000 ps, respectively. The color scale represents the square root of the normalized X-ray photon density on the Zyla detector. The ReLaX laser is incident from the right, as indicated by the white arrow in (e). The implosion event is indicated by the hollow black arrow in each panel. In (g), examples of a blast shock wave at the laser focus and a cylindrical compression shock wave on the wire surface are illustrated by the red and pink dashed curves, respectively. (i)–(k) A 25 μm Al wire at 700 ps delay for ReLaX laser energies of 1.35, 0.81, and 0.27 J, respectively. (l)–(n) Horizontal lineouts (without the square-root transform) taken at the positions indicated by the black arrow in (g) ($z = 41$ μm), the red arrow in (g) ($z = 111$ μm), and the red arrow in (i) ($z = 41$ μm), with each run's normalized pre-shot profile at the same position shown as the reference.

capability of the XFEL + femtosecond-laser platform for studying ICF-relevant high pressure physics at reduced scale.

II. EXPERIMENTAL SETUP

The experiment (p5689) was executed at the HED-HiBEF instrument[24] at the European X-ray Free Electron Laser, utilizing the ReLaX optical laser system (maximum power 300 TW) as the pump source. The ReLaX laser (with wavelength 800 nm) irradiated the targets at a 45° angle relative to the X-ray propagation axis. During the experiment, we measured that the energy in the center main Gaussian pulse was 1.35 J maximum (0.45 fraction of total 3 J), with a pulse duration under 25 fs. The focus on target had a full-width half-maximum (FWHM) of (5.6 ± 1.5) μm. The resulting maximum laser intensity was ~ 1.4×10^{20} W/cm². The 8.5 keV X rays generated by the SASE2 undulator were used to illuminate a quasi-Gaussian region (250 μm FWHM) around the ReLaX focal spot.

The target plane was imaged via a compound refractive lens stack of 15 beryllium lenses. Each lens had a radius of curvature of 50 μm with a web thickness of 30 μm. The focal length of the lens stack was 36 cm. The distance from the target to the imaging detector was 631 cm. The detector was a GAGG scintillator imaged to an Andor Zyla CMOS camera via either a 7.5× or a 2× objective. The detector pixel pitch was 6.5 μm. After accounting for the total magnification factor, this results in an equivalent pixel size on target of 56 nm/pixel for the 7.5× objective and 210 nm/pixel for the 2× objective.

The X-ray energy was characterized via elastic scattering on a Kapton foil with a von Hamos spectrometer. The pulse energy was ~700 μJ, measured with an X-ray gas monitor in the tunnel. Imaging resolution was determined using a resolution test target (NTT-XRESO 50HC). Data were collected in the self-seeded mode of the X rays, which provides improved spectral coherence and a narrow bandwidth (less than ~1 eV), resulting in a measured imaging resolution better than 200 nm.

The delay between the optical pump and the X-ray probe was scanned from a few picoseconds up to nanoseconds [one image per delay (single XFEL pulse per train)]. This allows imaging of the convergence of the implosion at different positions along the wire axis. A representative dataset is shown in Fig. 1, where the implosion dynamics of 10 and 25 μm copper wire and 25 μm Al wire are recorded at various time delays. Both the blast shock wave generated by the laser focal hotspot and the cylindrical shock wave emerging at the wire surface and compressing inward are clearly observed, as illustrated in Fig. 1(g). Implosion events resulting from cylindrical compression are indicated by hollow black arrows in each panel. The horizontal lineouts in Figs. 1(l)–1(n) reveal reduced transmission at the compressed region compared with the respective cold pre-shot references.

III. RETURN CURRENT SCALING LAW VALIDATION

A. Current density distribution on the wire surface

In Ref. 10, it was demonstrated that electrons escaping from an intense laser-irradiated target induce a return current flowing along the wire's surface. Owing to the ultrashort (~100 fs) duration of the current pulse, the return current is confined within the skin-depth layer of the target surface. The transient current rapidly heats this thin surface plasma layer to temperatures of several

hundred electron volts (eV) within a 100 fs timescale, while maintaining solid densities. The subsequent rapid ablation generates inward-propagating shocks, driving a cylindrical shock compression of the wire target. Given the extremely short duration of the current pulse, the surface plasma temperature can be treated as an initial condition for the subsequent hydrodynamic evolution. Consequently, a direct correspondence exists between the surface temperature, the current density, and the resulting implosion time. Building upon these relationships, we derive that the surface current density on a thin wire satisfies the return-current scaling law

$$\frac{j_2}{j_1} \approx \frac{r_1}{r_2}, \qquad (1)$$

where j_i and r_i are the current density and radius for two different wire configurations. We determine the *surface current density* j indirectly from the cylindrical implosion time τ_{im}: for a given surface temperature T_e, there is a one-to-one mapping $T_e \leftrightarrow \tau_{im}$ and $T_e \leftrightarrow j$, and so

$$j(z) = \mathscr{J}[T_e(\tau_{im}(z))].$$

It is shown that return currents have two main consequences for the wire target:[10] one is the Z-pinch effect, the other is the Joule heating effect. In the wire targets that we use here (with 10–25 μm diameter), the first effect can be ignored, since the magnetic pressure is much smaller than the ablation pressure. Thus, we can use the surface temperature to indirectly calculate the surface return current. To construct the mapping $f_1 : j \mapsto T_e$, we solve the electron-energy equation:[10]

$$\frac{3}{2} n_e \frac{\partial T_e}{\partial t} = \frac{1}{r} \frac{\partial}{\partial r} \left(r K_{T_e} \frac{\partial T_e}{\partial r} \right) + \frac{j(r)^2}{\sigma_{T_e}}, \qquad (2)$$

where K_{T_e} and $\sigma_{T_e} = n_e e^2 / (m_e \nu_{ei})$ are the electron thermal and electrical conductivities, respectively. For temperatures lower than 100 eV, the Burgess resistivity model is used,[25] while for temperatures higher than 100 eV, the SESAME conductivity is used.[26]

The full numerical solutions of Eq. (2) are shown in Fig. 2(a) for copper and aluminum ($d = 25$ μm) wires. For copper wires, the results for wire diameters of 10, 15, and 25 μm are identical and thus represented by a single curve. The weak radius dependence further confirms that Joule heating and heat transfer are limited in a very thin layer. The simulations cover peak current densities ranging from 5 to 200 kA/μm², with further details provided in Appendix A. As a guide, using the Spitzer resistivity[27] and neglecting radial heat conduction, we obtain

$$T_e^{5/2} - T_{e0}^{5/2} \simeq \frac{5}{3n_e} (1.03 \times 10^{-4} Z \ln \Lambda) j^2 \tau, \qquad (3)$$

and so, for $T_{e0} \ll T_e$, one has $T_e \propto j^{4/5}$ (i.e., $T_e \propto j^{0.8}$). This scaling is plotted as a dashed line in Fig. 2(a). It can be seen that there are modest deviations for those two temperatures at $j < 50$ kA/μm² (where the use of the Spitzer resistivity overestimates the collision rate) and at $j > 100$ kA/μm² (where radial heat transfer loss becomes significant).

Next, the mapping $f_2 : T_e \mapsto \tau_{im}$ is obtained from one-dimensional hydrodynamic simulations (see Appendix A and Refs. 9 and 10). In the ablation-driven, strong-shock limit [over ~100 Mbar
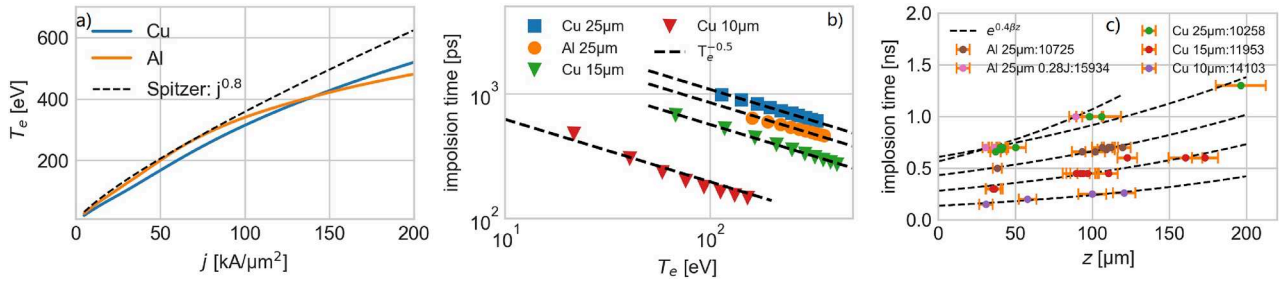
FIG. 2. (a) Variation of target surface temperature with peak current density. The dashed line shows the temperature–current density scaling according to the Spitzer resistivity model. (b) Variation of target implosion time with surface temperature obtained from 1D hydrodynamic simulations. The dashed lines show the strong shock wave scaling. (c) Target implosion time along the wire z position obtained from experimental measurements. The dashed lines show exponential fits of the data. The default laser energy is 1.35 J. The fitted β are shown in each curve label. The initial conditions of Cu wires indicated by X-ray spectroscopy in Appendix F show good consistency. The 25 μm Al data with 0.28 J laser energy at 1 ns delay have a misalignment.

and ~100 eV in the skin depth layer; see Figs. 2(a) and 2(b)], the Rankine–Hugoniot relation results in a shock velocity that scales as $U_s \propto T_e^{1/2}$. As an approximation for small-radius targets, the average shock velocity $\overline{U_s} \propto U_s$, and so

$$\tau_{im} = \frac{r_0}{\overline{U_s}} \propto T_e^{-1/2}. \tag{4}$$

Figure 2(b) shows $\tau_{im}(T_e)$ for different wire geometries, with dashed lines indicating the $T_e^{-0.5}$ fit. All four cases exhibit a strong agreement between the fitting and the simulation data. The simulations suggest that the implosion process is a strong shock process driven by the surface ablation. Thus, the initial surface temperature distribution after surface-return-current heating along the wire position z can be obtained by incorporating the experimentally measured implosion time τ_{im}.

Finally, the mapping $f_3 : (z, \tau_{im}) \mapsto j(z)$ is extracted from experimental measurements of implosion time vs axial position (assuming that the laser focus is $z = 0$ μm) as shown in Fig. 2(c). Details of the experimental data extraction procedure and the derivation of error bars are given in Appendix B. Owing to the recirculation of hot electrons,[18,28–31] target bulk displaced from the laser focal spot can experience a bulk return current (the compensating bulk electron flow when hot electrons pass through the bulk) Joule heating induced by laser-accelerated hot electrons.[32] We employ 2D full-scale hydro–PIC simulations constrained by the measured ReLaX contrast and intensity (FLASH → PIConGPU; see Appendix D) to evaluate the wire's bulk temperature. Combined with global energy conservation and phase-contrast imaging (PCI) forward calculations[33] presented in Appendix E, these results indicate that at an offset of 30 μm, the bulk temperature remains at or below 2 eV (see Appendix E). Appendix F shows raw Cu K-α spectra dominated by the neutral doublet with only a weaker ionized-Cu complex, indicating that the line-of-sight emission is bulk-dominated by near-neutral material and supporting our assumption that the bulk away from the focus can be treated as effectively cold. Under these conditions, the corresponding correction to the surface-shock velocity is of order 1% [see Eq. (E3)] and is neglected.

Therefore, we consider implosion data acquired from regions located beyond 30 μm from the focal spot, and thus assume a cold initial state for the analysis presented in this work. As the return

current propagates along the wire surface with surface wave behavior, the current density along the z position of the wire propagates with[33,34]

$$j(z, t) \propto j_0(z - v_g t) \exp(-\beta z), \tag{5}$$

where j_0 is the initial current density at $z = 0$, β is the decay constant associated with wire impedance, and v_g is the group velocity of the surface current wave. By incorporating Eqs. (3)–(5), we have

$$\tau_{im}(z) \propto \exp(0.4\beta z), \tag{6}$$

showing that the implosion time distribution $\tau_{im}(z)$ is exponentially increasing with z position. The dashed lines in Fig. 2(c) represent the fitting of the experimental data using Eq. (6). The strong agreement between the experimental data and the fitting confirms the surface wave behavior on the wire targets. Because the decay constant β represents impedance attenuation along the wire surface, it depends primarily on geometry, material properties, and wave frequency—conditions that were similar across all our experimental cases. Consequently, all cases exhibit very similar decay constants, as illustrated in Fig. 2(c). This characteristic enables reconstruction of the current density distribution on the target surface using limited experimental data, making a systematic validation of the scaling law feasible. We reconstruct the initial surface temperature and the peak surface current density profile along the wire as shown in Fig. 3. Having reconstructed the current-density profile along the wire, we next examine how this profile's characteristics scale with wire radius, material, and laser energy.

B. Current density radius and atomic-number dependence

Figures 3(a) and 3(b) present the reconstructed initial surface temperature and peak current density distributions for Cu and Al wires of various radii irradiated by a 1.35 J laser (shown as data points). Figures 3(c) and 3(d) show the corresponding results for Al wires of fixed diameter (25 μm) under various laser energies. The dashed curves represent exponential fits based on the surface wave model described by Eq. (5). For the radius-scaling cases, separate fitting constants are used for each curve, as indicated in the figure labels. For the energy-scaling cases, the curve corresponding to the 1.35 J, 25 μm Al wire is used as a baseline and linearly scaled to
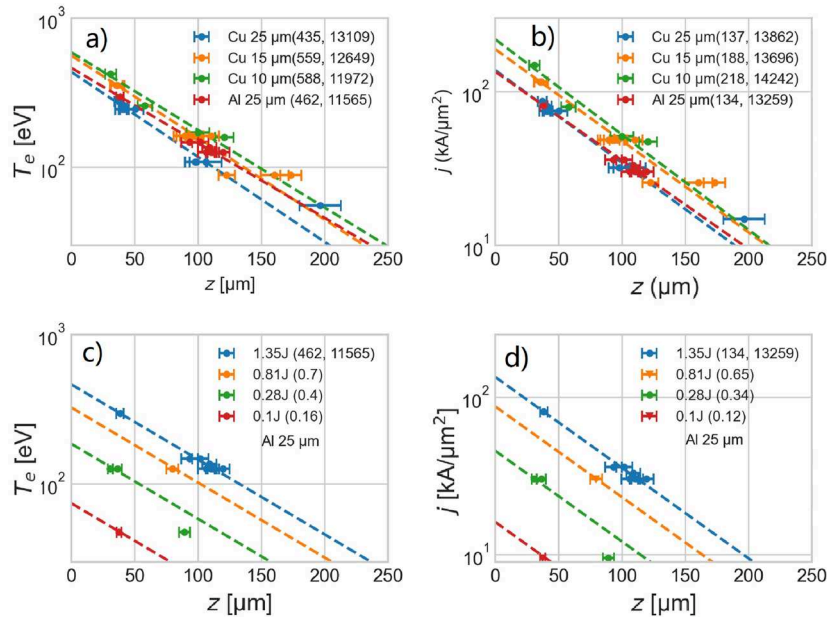
FIG. 3. (a) and (c) Reconstructed initial surface temperature. (b) and (d) Reconstructed peak surface current density j along the wire axis z. Data points with error bars represent values obtained from Fig. 2. Dashed lines show exponential fits $y(z) = \alpha \exp(-\beta z)$ to the reconstructed data. The two numbers in parentheses in each label denote the fitting constants: α [units of eV for (a) and (c), and kA/μm² for (b) and (d)] and β (units of m⁻¹), respectively. (c) and (d) show results rescaled to the 1.35 J, 25 μm Al wire reference case; in these panels, the single number in parentheses in each label is the normalization factor.

other laser energies. As shown in Figs. 3(a) and 3(b), the experimental data largely follow the fitted exponential profiles within the first 100 μm of axial position. Beyond this range, the measured values tend to slightly exceed the model predictions, with noticeably larger uncertainties. This discrepancy arises because the Spitzer resistivity model deviates from its $T^{-3/2}$ scaling at lower temperatures (below 100 eV in our study). Overall, the agreement between experiment and theory supports the exponential attenuation behavior described in Sec. III A.

Using the 25 μm Cu wire as reference, Fig. 3(b) shows that for smaller-radius Cu wires (15 and 10 μm), the current density at a given position increases as the wire radius decreases, consistent with the expected scaling law trend. However, when considering the actual ratio, the radius-scaling law predicts $r_{25}/r_{15} \approx 1.67$, whereas the experiment gives $j_{15}/j_{25} \approx 1.35$ (~19% lower), and for 10 μm wires, it predicts $r_{25}/r_{10} \approx 2.50$ vs the measured 1.65 (~34% lower) for the $z = 40$ μm position. It is found that the nominal inverse-radius scaling $j \propto r^{-1}$ overestimate the current density when scaling from a large-radius to smaller-radius target. The correction for the nominal scaling law can be studied from at least two aspects. First, according to the target normal sheath acceleration (TNSA) mechanism, a sheath field forms at the target surface, and only hot electrons with energies exceeding the sheath potential can escape;[18,28–31] the magnitude of the sheath field depends on the target geometry. The sheath field intensity at the rear of the target scales as $E \propto d^{-2}$ for a slab target,[35] implying that increased target thickness reduces hot-electron recirculation and enhances hot-electron escape as the wire diameter increases. Under ideal conditions, with no pre-plasma of target and hydrogen atoms, we infer that the reduced

escaping-electron charge in thinner wires leads to a current density ratio correction $\phi(r) = (r/25 \text{ μm})^{0.49}$, as confirmed by the analytic calculation presented in Appendix C.

Realistic laser contrast introduces pre-pulse preheating and pre-expansion that modify both laser absorption and hot-electron escape. According to 2D full-scale hydro–PIC simulations (FLASH → PIConGPU; details of which are given in Appendix D), the resulting total escaping hot-electron number N_{es}, laser-absorption coefficient A_L, and escape fraction $f_{es} \equiv N_{es}/N_h$—evaluated across materials, radii, and laser energies—are summarized in Fig. 4, where N_h denotes the total hot-electron yield produced under absorption A_L. For Cu wires (laser energy 1.35 J), the PIC results show that N_{es} increases with radius—consistent with the ideal trend—but the effective radius correction is stronger, with $\phi(r) = (r/25 \text{ μm})^{0.47}$ (fit over 10–25 μm); see Fig. 4(a). Since $N_{es} \propto A_L f_{es}$, we separate absorption and escape: the absorption varies only slightly with radius [$A_L \simeq 0.20$ for 10 μm and $A_L \simeq 0.23$ for 25 μm; Fig. 4(b), circles], indicating that the primary source of the radial dependence of N_{es} is the escape fraction f_{es} [Fig. 4(b), squares]. Consequently, the realistic pulse shape and target pre-expansion introduce additional corrections beyond the ideal prediction in Fig. 7(b) (Appendix C), reconciling the observed departures from the nominal r^{-1} law.

Second, variations of the current density decay constant β across radii and materials would introduce an additional correction to the scaling. We quantify propagation losses by defining β via a single-exponential attenuation of the surface current, $j(z) = j_0 \exp(-\beta z)$, and extracting β from a linear fit to $\ln j(z)$ over the same z window (0–250 μm) for all cases at fixed incident energy 1.35 J as shown in Fig. 3(b). The fitted attenuations β are
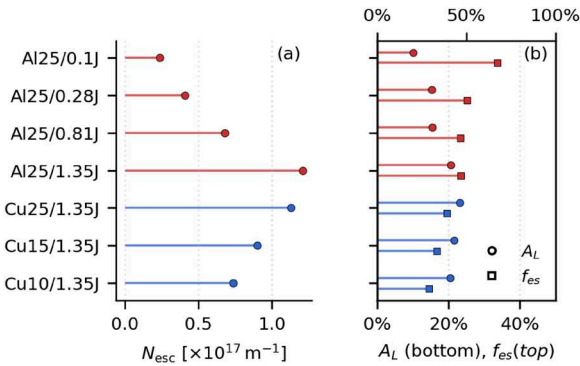
FIG. 4. Full-scale hydro-PIC simulation results for laser absorption and hot-electron escape. (a) Escaped hot-electron line density N_{esc} ($\times 10^{17}$ m^{-1}) for each target/energy condition (vertical-axis labels on the left); colors encode the material (Cu = blue, Al = red). (b) Same category order; circles show laser absorption A_L referenced to the *bottom* horizontal axis (0%–50%), while squares show the hot-electron escape fraction f_{esc} referenced to the *top* horizontal axis (0%–100%). Markers are slightly offset vertically for readability, but correspond to the same vertical-axis category.

$\beta_{25}^{Cu} = 1.3862 \times 10^4$ m^{-1}, $\beta_{15}^{Cu} = 1.3697 \times 10^4$ m^{-1}, $\beta_{10}^{Cu} = 1.4242 \times 10^4$ m^{-1}, and $\beta_{25}^{Al} = 1.3260 \times 10^4$ m^{-1}. These cluster around $\bar{\beta} \simeq 1.38 \times 10^4$ m^{-1} with a spread of only a few percent (−1.2%, +2.7%, and −4.3% relative to β_{25}^{Cu}). Hence, under identical pulse conditions, attenuation differences are modest and subdominant to the geometric escape correction $\phi(r)$ introduced above. We note that the value of β reported here is slightly different from that in Fig. 2(c) because Eq. (6) was derived assuming a Spitzer-resistivity scaling, $T_e \propto j^{0.8}$. As shown in Fig. 2(a), this scaling breaks down at both low and high current densities; consequently, the inferred β deviates accordingly.

Combining those two corrections, the ratio of current densities at two radii r_1 and r_2 becomes

$$\frac{j_{r_1}(z)}{j_{r_2}(z)} = \frac{r_2}{r_1}\phi(r_1, r_2)\exp\left[(\beta_{r_1} - \beta_{r_2})z\right] \approx \left(\frac{r_2}{r_1}\right)^{0.53}\exp\left[(\beta_{r_1} - \beta_{r_2})z\right], \tag{7}$$

where $\phi(r_1, r_2) = (r_1/r_2)^{0.47}$. Equation (7) captures the data quantitatively. At $z = 40$ µm, for example, we obtain $j_{15}/j_{25} \approx 1.30$ vs 1.35 fitted measured and $j_{10}/j_{25} \approx 1.65$ vs 1.60 fitted measured, i.e., agreement at three-percent level. Hence, Eq. (7) serves as a compact, accuracy-level description of the radial scaling in the present regime.

With geometric effects excluded, for a cylindrical conductor (radius r) at surface current angular frequency ω, the surface maximum surface current density is

$$J_{max} = \frac{Ik}{2\pi a}\frac{J_0(kr)}{J_1(kr)} \approx \frac{I}{2\pi a\delta_{eff}} \qquad \text{for} \quad |k|r \gg 1, \tag{8}$$

with $k = (1 + i)/\delta_{eff}$, where $J_{0,1}$ are Bessel functions of the first kind, I is the total current, and δ_{eff} is the effective skin depth. We choose $\delta_{eff} = \min(\delta_R, \delta_P)$, where the resistive skin layer $\delta_R = \sqrt{2/(\mu_0\omega\sigma)}$ and the plasma skin layer $\delta_P = c/\sqrt{\omega_p^2 - \omega^2} \simeq c/\omega_p$ ($\omega \ll \omega_p$). For Spitzer transport, $\eta \simeq 1.03 \times 10^{-4} Z \ln\Lambda/T_e^{3/2}$ (SI; T_e in eV), and so $\sigma = 1/\eta$ and $J_{max} \propto (I/2\pi r)(\sigma\omega)^{1/2} \propto (I/2\pi r)T_e^{3/4}(Z\ln\Lambda)^{-1/2}\omega^{1/2}$.

when $\delta_{eff} = \delta_R \ll r$. Figure 3(b) compares the reconstructed $j(z)$ for 25 µm Cu and Al wires, yielding $j(z)_{Cu}/j(z)_{Al} \approx 1$ across the measured range. This near-unity ratio shows that under identical geometrical and laser conditions, the return-current scaling law is weakly Z dependent for the Cu and Al wires. Two key factors explain this result: first, the initial amplitude $I = dN_{es}/dt$ is governed predominantly by wire geometry (radius) rather than atomic number, as shown in Fig. 4(a); second, Cu and Al follow nearly identical Spitzer-resistivity models at our experimental temperatures.[33] Consequently, the surface return currents are largely insensitive to material choice under our conditions. To more stringently test the material dependence of the surface-return-current scaling, future measurements including a low-Z polymer (CH) and a high-Z metal (W) would be informative.

In summary, the surface-return-current density increases systematically as the wire radius decreases, and the measured ratios are captured within a few percent by the revised scaling [Eq. (7)] once the escape factor $\phi(r)$ and the radius-tagged attenuation β are included. By contrast, Cu and Al wires of identical diameter yield indistinguishable $j(z)$, indicating only a minimal Z dependence in our parameter range (Cu vs Al, with geometry and drive held fixed). Building on these findings, in Sec. III C, we isolate geometric and material effects by studying a single 25 µm Al wire under varying laser energies, thereby assessing the potential of ultrashort-pulse lasers for fusion-relevant pressure generation.

C. Current density laser energy dependence

Understanding how the surface-return-current density scales with incident laser energy is critical for extrapolating from the current ReLaX system—which approaches ~1 Gbar pressures (pressure at implosion stagnation based on hydro simulations)[9,10]—to the higher energies required for ICF-relevant high pressures. We therefore systematically study the dependence of j on E_L (laser energy).

The dependence of the surface-return-current density on incident laser energy follows the hot-electron temperature scaling in Eq. (C2). We compare the measurements with three established scalings: Kluge's,[36] the ponderomotive (Wilks) scaling,[37] and Beg's experimental scaling.[38] Within our high-contrast, femtosecond drive window ($a_0 \in [1.0, 8.25]$), Kluge's and Beg's scalings show the closest agreement with the PIC results and experimental data,[36] whereas the ponderomotive trend does not reproduce the observed energy dependence as well.[36] Because Beg's original fit pertains to picosecond-duration pulses with substantial preplasma, we use Kluge's scaling as a neutral baseline for extrapolation and for normalizing the amplitude trends, while retaining Beg's and ponderomotive curves for reference. For completeness, we can have an analytic equation for the current density laser energy dependence with Beg's scaling. Using $T_h = 0.469a_0^{2/3}$[38] and Eq. (C2), we obtain

$$j \propto E_L^{2/3} w_0^{-4/3} \tau_L^{-2/3}, \tag{9}$$

where w_0 is the laser focus waist and τ_L is the laser pulse width. Those two parameters are fixed in our experiments. Hence, $j \propto E_L^{2/3}$ when w_0 and τ_L are held constant.

Figure 5 summarizes the amplitude factors C extracted from the axial fits $j(z) = Ce^{-\beta z}$ for a 25 µm Al wire at
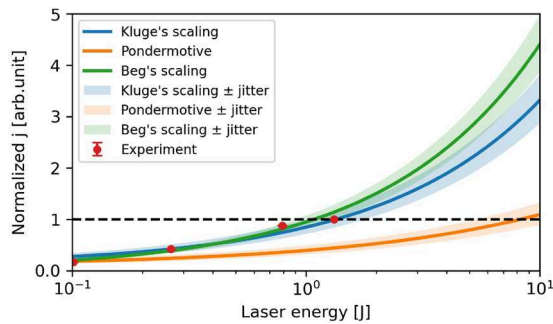
FIG. 5. Variation of surface-return-current density in 25 μm Al wire with laser energy. Here, the laser waist and pulse duration are fixed. Shot-to-shot focusing jitter causes the focal FWHM radius to fluctuate around 5.6 μm with a spread of 1.5 μm [i.e., $w_0 = 5.6(15)$ μm].

$E_L = \{1.35, 0.81, 0.28, 0.10\}$ J, yielding $C = \{1.00, 0.65, 0.34, 0.12\}$ [see also Figs. 3(c) and 3(d)]. The apparent energy dependence is influenced by the nanosecond/picosecond pre-pulse levels, which vary with energy at fixed contrast in those experiments, and to compare with hot-electron temperature scalings, we renormalize C by the simulated laser absorption A_L and escape fraction f_{es} (Fig. 4). The experimental curve is co-registered to Kluge's scaling at 1.35 J, and the ordinate is normalized such that this common reference equals unity. The theoretical bands include the ReLaX shot-to-shot focus spot jitter. Over the explored intensity range, the renormalized data follow Kluge's and Beg's scalings closely, while ponderomotive predicted trends do not follow the measured current density at higher laser intensities. This establishes that hot-electron dynamics reliably predict the peak return current and, by extension, the attainable pressure as a function of laser energy. When the full energy of the ReLaX laser (typically 10 J per pulse) is utilized in future experiments, the peak surface current density is expected to increase by a factor of approximately three compared with the 1.35 J case, based on the experimentally validated scaling law. For a 25 μm Cu wire, this corresponds to a surface temperature of ~500 eV at an axial offset of 40 μm from the laser focal position. Hydrodynamic simulations predict that the resulting stagnation pressure could reach up to 2 Gbar under these conditions.

This scaling indicates that by increasing the laser energy, one can predictably raise the peak return current (and thus implosion pressure), informing the design of next-generation high-energy experiments.

IV. SUMMARY AND OUTLOOK

Our experiments have provided the first systematic validation of return-current-driven implosion scaling, demonstrating clear dependencies on wire diameter, material, and laser energy. The comprehensive study demonstrates clear scaling behaviors with wire diameter, material, and laser energy.

The residual deviation from $j \propto r^{-1}$ is quantitatively explained by the radius-dependent escape fraction $\phi(r)$ (capacitive-sheath effect) and, to a lesser extent, small differences in current attenuation β; together they yield Eq. (7), which matches the measured ratios at the 3% level.

These findings bridge a critical gap between theoretical models and experimental observations. The refined scaling laws greatly enhance our ability to predict implosion dynamics, which is essential for the development of ICF technology and HED plasma science. By confirming these scaling laws, we provide a solid experimental foundation for designing future high-energy experiments and for benchmarking simulation codes in HED physics.

AUTHOR DECLARATIONS

Conflict of Interest

The authors have no conflicts to disclose.

Author Contributions

L.Y. conceived the original idea and developed the theoretical framework. A.L.G. and T.T. laed the experiment. L.Y., C.B., V.B., E.B., T.D., N.F., T.G., S.G., J.H., H.H., L.G.H., O.H., T.K., D.K., J.L., J.P.N., M.N., A.P., T.R.P., C.B.Q., S.V.R., R.R., M.R., L.R., J.J.S., M.Š., U.S., J.P.S., M.V., U.Z., K.Z., A.L.G., T.T., and T.E.C. conducted the experiment. M.L.H. processed the experimental data. L.Y. carried out the PIC and hydrodynamic simulations. L.Y., M.L.H., L.G.H., A.L.G., T.T., and T.E.C. performed the data analysis. A.L.G. and T.T. wrote the experimental section of the paper. L.Y. wrote the remaining sections. T.E.C. contributed to the concept presented in Appendix C. All authors discussed the results and reviewed the manuscript. T.E.C. supervised the project.

L. Yang: Conceptualization (lead); Writing – original draft (lead). **M.-L. Herbert**: Data curation (equal); Writing – original draft (equal); Writing – review & editing (equal). **C. Baehtz**: Investigation (equal); Writing – review & editing (equal). **V. Bouffetier**: Investigation (equal); Writing – review & editing (equal). **E. Brambrink**: Investigation (equal); Writing – review & editing (equal). **T. Dornheim**: Investigation (equal); Writing – review & editing

05 February 2026 10:38:38

(equal). **N. Fefeu**: Investigation (equal); Writing – review & editing (equal). **T. Gawne**: Investigation (equal); Writing – review & editing (equal). **S. Goede**: Investigation (equal); Writing – review & editing (equal). **J. Hagemann**: Investigation (equal); Writing – review & editing (equal). **H. Höppner**: Investigation (equal); Writing – review & editing (equal). **L. G. Huang**: Investigation (equal); Writing – original draft (equal); Writing – review & editing (equal). **O. Humphries**: Investigation (equal); Writing – review & editing (equal). **T. Kluge**: Investigation (equal); Writing – review & editing (equal). **D. Kraus**: Investigation (equal); Writing – review & editing (equal). **J. Lütgert**: Investigation (equal); Writing – review & editing (equal). **J.-P. Naedler**: Investigation (equal); Writing – review & editing (equal). **M. Nakatsutsumi**: Investigation (equal); Writing – review & editing (equal). **A. Pelka**: Investigation (equal); Writing – review & editing (equal). **T. R. Preston**: Investigation (equal); Writing – review & editing (equal). **C. B. Qu**: Investigation (equal); Writing – review & editing (equal). **S. V. Rahul**: Investigation (equal); Writing – review & editing (equal). **L. Randolph**: Investigation (equal); Writing – review & editing (equal). **R. Redmer**: Investigation (equal); Writing – review & editing (equal). **M. Rehwald**: Investigation (equal); Writing – review & editing (equal). **J. J. Santos**: Investigation (equal); Writing – review & editing (equal). **M. Šmíd**: Investigation (equal); Writing – review & editing (equal). **U. Schramm**: Investigation (equal); Writing – review & editing (equal). **J.-P. Schwinkendorf**: Investigation (equal); Writing – review & editing (equal). **M. Vescovi**: Investigation (equal); Writing – review & editing (equal). **U. Zastrau**: Investigation (equal); Writing – review & editing (equal). **K. Zeil**: Investigation (equal); Writing – review & editing (equal). **A. Laso Garcia**: Investigation (equal); Project administration (equal); Writing – original draft (equal); Writing – review & editing (equal). **T. Toncian**: Investigation (equal); Project administration (equal); Writing – original draft (equal); Writing – review & editing (equal). **T. E. Cowan**: Conceptualization (equal); Supervision (lead).

DATA AVAILABILITY

The raw experimental data are available at https://doi.org/10.22003/XFEL.EU-DATA-005689-00 upon reasonable request. Additional data that support the findings of this study are available from the corresponding authors upon reasonable request.

APPENDIX A: HYDRODYNAMIC SIMULATIONS

Hydrodynamic simulations were performed using the FLASH code (version 4.6.2), developed by the University of Rochester.[39,40] All simulations were carried out in one-dimensional cylindrical geometry. The computational domain spanned 50 μm in radius, with the target occupying the central region and the remainder initialized as vacuum. To facilitate numerical stability, the vacuum region was filled with low-density hydrogen (1×10^{-5} g/cm^3) at a temperature of 1 eV. Target materials were copper and aluminum, each initialized at their respective solid densities.

On ~ 100 fs timescales, heat transport along the wire axis (z) is negligible. We therefore model the implosion as a one-dimensional radial hydrodynamic evolution, with the surface temperature governed by surface return current Joule heating via Eq. (2). The target is initialized at solid density with a uniform temperature $T_0 = 0.1$ eV on a radial grid with spacing $\Delta r = 3.125$ nm, for a set of initial wire
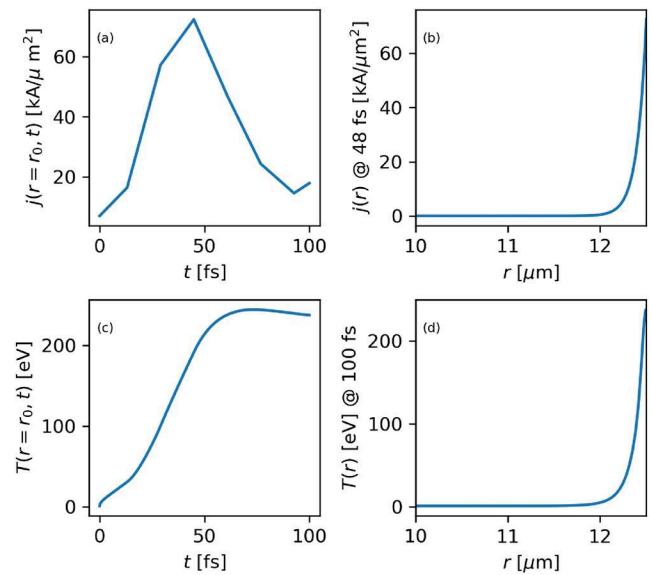

FIG. 6. (a) Example of a surface-return-current waveform for a case with peak intensity of 80 kA/μm^2. (b) Radial current-density profile $j(r)$ at t = 48 fs for a 25 μm Cu wire. (c) Corresponding surface temperature history. (d) Radial temperature profile at t = 100 fs.

radii. The 100 fs surface-return-current waveform at $r = r_0$ (with r_0 the initial wire radius) is taken from Ref. 10 and an example is shown in Fig. 6(a) for a peak intensity of 80 kA/μm^2. The radial current density $j(r,t)$ is obtained from a skin-depth prescription; an example for a 25 μm Cu wire at $t \approx 48$ fs is plotted in Fig. 6(b). The corresponding surface peak temperature is shown in Fig. 6(c), and the radial temperature profile at t = 100 fs is shown in Fig. 6(d). These temperature profiles are then used as initial conditions for FLASH hydrodynamic simulations to determine the implosion time corresponding to a given peak surface temperature and current density. Finally, we scale the applied current density to different peak values to map the resulting surface temperatures and implosion times.

Figure 2(a) shows the calculated peak surface temperature for different current densities. In accordance with the return-current scaling theory,[10] the magnetic compression associated with the $\mathbf{J} \times \mathbf{B}$ force is neglected, and the initial fluid velocity is set to zero. Reflective boundary conditions are applied at the symmetry axis, while outflow boundary conditions are used at the outer edge of the simulation domain. A self-adaptive mesh refinement scheme is employed to resolve steep gradients. Material properties are obtained from SESAME equation-of-state tables.[26] The system is evolved using the one-fluid, two-temperature (ion and electron) hydrodynamic equations implemented within FLASH. The simulated implosion times corresponding to different initial surface temperatures are shown in Fig. 2(b).

APPENDIX B: OBTAINING IMPLOSION TIME FROM EXPERIMENTAL DATA

Here, the laser irradiation position and wire implosion position have to be determined by analyzing the detector images as shown

in Fig. 1. The position of the shock convergence point can be read-off directly, while the laser irradiation position has be determined using the mean value of the edges of the circular region around the laser impact. We have selected three datasets for this study. The first dataset comprises Cu wires with different radii (25, 15, and 10 μm) and is used to investigate the radial dependence of the current density. The second dataset includes 25 μm wires made of different materials, specifically Cu and Al, to verify the atomic number (Z) dependence of the current density. The third dataset consists of 25 μm Al wires irradiated by different incident laser energies (1.35 J as the default, and 0.81, 0.28, and 0.1 J) to examine the laser energy dependence of the current density. Each dataset includes repeated runs with different XFEL delays relative to the ReLaX laser irradiation time. For each effective run, an implosion point is observed on the wire. The z position of this implosion point is measured for each corresponding delay, resulting in pairs of z positions and implosion times. A summary of the variation in wire implosion time with z position is presented as the data points in Fig. 2. The error bars come from the detector's resolution, from inaccuracies when reading off the positions due to low contrast in some cases or the size of the relevant features on the image, and from the conversion of pixels to μm.

APPENDIX C: NONIDEAL EFFECTS OF ESCAPING CHARGES: DEPENDENCE ON TARGET RADIUS

In this appendix, we discuss the nonideal effects of the escaping charges as a function of the target radius. Outside the target wire, the hot-electron density is assumed to follow a Boltzmann distribution

$$f(E) = \frac{1}{k_B T_h} \exp\left(-\frac{E}{k_B T_h}\right), \tag{C1}$$

where T_h is the hot-electron temperature. The total number of hot electrons is given by

$$N_h = A_L \frac{E_L}{T_h}, \tag{C2}$$

with A_L representing a laser absorption coefficient and E_L the laser energy. Hot electrons with energy $E > eV_s$ (where V_s is the sheath potential) escape from the target. Consequently, the fraction of escaping charges is

$$f_{es} = \frac{N_{es}}{N_t} = \int_{eV_s}^{\infty} f(E)\, dE = \exp\left(-\frac{eV_s}{k_B T_h}\right), \tag{C3}$$

which indicates that only those hot electrons with energies exceeding the sheath potential V_s overcome the barrier and escape into vacuum. Simultaneously, these escaping electrons contribute to an increase in the sheath potential.

The potential generated by the hot electrons in a cylindrical system can be derived from the Poisson equation in vacuum,

$$\frac{1}{r}\frac{d}{dr}\left(r\frac{dV}{dr}\right) = \frac{en_e}{\varepsilon_0}. \tag{C4}$$

To simplify the analysis, an effective capacitance, C_{eff} is introduced so that the sheath potential is given by

$$V_s = \frac{Q_{es}}{C_{eff}}, \tag{C5}$$

where $Q_{es} = eN_{es}$ is the escaping charge. Thus, Eq. (C3) becomes

$$f_{es} = \exp\left(-\frac{e^2 N_{es}}{C_{eff} k_B T_h}\right) = \exp\left(-\frac{e^2 f_{es} N_h}{C_{eff} k_B T_h}\right). \tag{C6}$$

The solution of this equation yields

$$f_{es}(r) = \frac{C_{eff}(r)(k_B T_h)^2}{A_L e^2 E_L} W\left(\frac{A_L e^2 E_L}{C_{eff}(r)(k_B T_h)^2}\right), \tag{C7}$$

where $W(\cdot)$ is the Lambert W function. Moreover, solving Eq. (C4) leads to the unit capacitance of a wire target,

$$C(r) = \frac{2\pi\varepsilon_0}{\ln(1 + r_1/r)}, \tag{C8}$$

with r being the radius of the cylinder and r_1 the effective radius of the outer conductor. In our case, the surface return current is supplied by short-range hot electrons escaping from the target. Thus, r_1 denotes the short-range hot-electron escape distance and is set by the pulse duration, $r_1 \sim c\tau_L$, where τ_L is the laser pulse duration and c is the speed of light.

From Eq. (C7), it can be shown that

$$f_{es}(L_0, r) \propto L_0 C(r) W(f_w(L_0, C(r))) \approx L_0 C(r) W(f_w(L_0)), \tag{C9}$$

where f_w is the collection of terms inside the Lambert W function as shown in Eq. (C7), L_0 is the effective length of the capacitance, and $C_{eff} = L_0 C(r)$. The approximation in Eq. (C9) is made because r is only a small perturbation compared with L_0. Thus, the trend of variation of $f_{es}(L_0, r)$ with the target radius is decoupled from the target length L_0, enabling us to use two-dimensional PIC simulations to verify this result.

The theoretical prediction for the escaping charges, based on Eq. (C7) (with $r_1 = 1$ μm), is shown as a solid line in Fig. 7. The results indicate that the target radius has only a minor effect on the escaping charges. An exponential function of the form r^x was used to fit the data (the dashed line in Fig. 7), yielding an exponent of 0.49. This dependence of the escaping charges on the radius consequently reduces the scaling effect of the target radius on the surface return current.
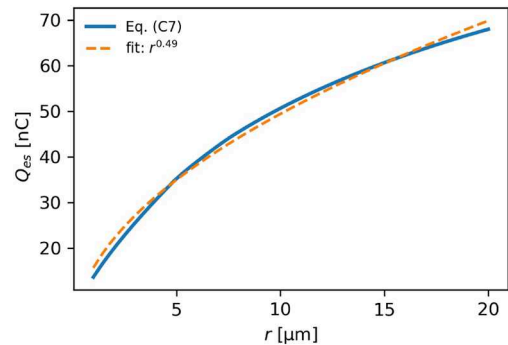

FIG. 7. Escaping charges as calculated analytically using Eq. (C7) at a laser energy of 1.35 J. The dashed line shows a curve fitting to the analytical results.

APPENDIX D: ESCAPING CHARGES WITH FULL-SCALE HYDRO–PIC SIMULATIONS

The ReLaX temporal contrast is not an ideal Gaussian: a pre-pulse of intensity $\sim 1 \times 10^{10}$ W/cm^2 appears $\sim$100 ps before the main peak [Fig. 8(a)], preheating and slightly pre-expanding the wire surface. This pre-expansion can affect both main-pulse coupling and hot-electron escape. We therefore use FLASH to model the pedestal/prepulse and feed the resulting density profile into PIConGPU[41] for the femtosecond interaction.

For the hydro stage (FLASH), field ionization of Cu/Al becomes important only near $\sim 1 \times 10^{13}$ W/cm^2 on $\sim$10 ps timescales before the main pulse;[42] we therefore start at $t = -100$ ps (intensity $\sim 1 \times 10^{10}$ W/cm^2) and evolve the rising edge until it reaches 1×10^{16} W/cm^2 at $t \approx -(0.3$–$0.4)$ ps (based on laser energy). Over this last 0.3–0.4 ps the hydrodynamic expansion is quasi-static; we freeze the density profile at $t = -(0.3$–$0.4)$ ps and use it as the initial condition for the PIC stage. The preplasma scale length (for the example of a 25 μm Cu wire with 1.35 J laser energy) at the $\lambda = 800$ nm critical surface is $\sim$700 nm [Fig. 8(b)], and a two-dimensional density map for Al at $t = -0.3$ ps is shown in Fig. 8(c). FLASH uses two-dimensional Cartesian with outflow boundaries and SESAME EOS tables (Cu/Al).

For the PIC stage (PIConGPU version 0.7.0, 2D3V), we include ionization and a Coulomb collision process. The targets are initialized at base densities of $34.6n_c$ (Al) and $48n_c$ (Cu), both with an initial charge state $Z = 1$. The simulation box is 60×60 μm^2; the laser propagates along x, is p-polarized, and is directed to an off-axis position $R/2$ from the wire center [Fig. 8(c)]. The grid spacing is 800 nm/194.56 (resolving plasma oscillations up to $n_e \sim 1400n_c$), with five macroparticles per cell. Absorbing (open) boundaries are used for fields and particles. For Al (the example shown), the

electron density at $t = 60$ fs (with $t = 0$ defined when the peak intensity reaches the wire surface) is plotted in Fig. 8(d); the corresponding E_y and mean kinetic energy $\frac{2}{3}\overline{E_k}$ are shown in Figs. 8(e) and 8(f), respectively. The sheath field peaks at $\sim$2 MV/μm, and the average hot-electron energy spans hundreds of keV to several MeV. Virtual detectors on the box boundaries record the escaping-electron spectra [Fig. 8(g)], and the total escaping number N_{es} vs simulation time with different materials, laser energies, and wire radii is shown in Fig. 8(h). These data are used to normalize the return current scaling laws in the main text.

APPENDIX E: VERIFICATION OF STRONG-SHOCK ASSUMPTION

Our inference of the surface-return-current density relies on the strong-shock assumption. We consider the unshocked bulk (state 1) with (ρ_1, P_1, T_0) as the upstream and the hot surface layer (state 2) with (ρ_2, P_2) as the downstream. The upstream sound speed is $c_0 = \sqrt{\gamma P_1/\rho_1}$, where γ is an effective adiabatic index. Using the Rankine–Hugoniot relations, we obtain

$$U_s^2 = c_0^2 \left[1 + \frac{\gamma + 1}{2\gamma} \left(\frac{P_2}{P_1} - 1 \right) \right] = \frac{\gamma + 1}{2\rho_1} P_2 + \frac{\gamma - 1}{2\rho_1} P_1. \quad \text{(E1)}$$

Equation (E1) shows that the shock speed is dominated by the downstream pressure P_2 (set by the surface layer), with a small additive correction from the upstream state P_1. In the strong-shock limit $P_2 \gg P_1$,

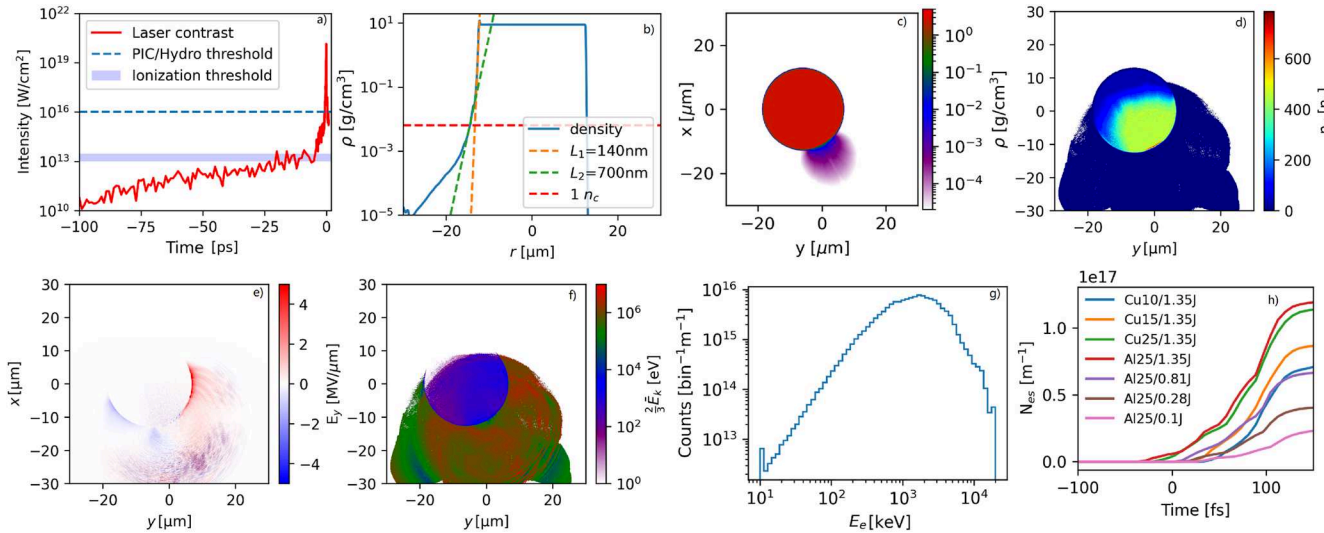$$U_{s0}^2 = \frac{\gamma + 1}{2\rho_1} P_2, \quad \text{(E2)}$$

FIG. 8. (a) Measured ReLaX laser temporal contrast. (b) Simulated Cu wire cross-sectional mass density at the laser focus, 400 fs before the main-pulse peak (laser energy 1.35 J). (c) Two-dimensional density map for Al at 400 fs before the main-pulse peak (laser energy 1.35 J). (d) Example of an Al electron-density snapshot at $t = 60$ fs (with $t = 0$ defined when the peak intensity reaches the wire surface). The ionization state can be overestimated owing to the temperature definition during the PIC simulation. (e) and (f) Corresponding transverse electric field E_y and average electron kinetic-energy distributions. (g) Energy spectrum of escaping hot electrons (25 μm Al wire, 1.35 J, 150 fs). (h) Total escaping number N_{es} as a function of simulation time for different materials, laser energies, and wire radii.

and the relative deviation induced by a finite bulk temperature (finite P_1) is

$$\frac{\Delta U_s}{U_{s0}} = \frac{U_s - U_{s0}}{U_{s0}} \simeq \frac{1}{2}\frac{\gamma-1}{\gamma+1}\frac{P_1}{P_2} \approx \frac{1}{4}\frac{P_1}{P_2} \qquad (\gamma = 5/3). \qquad \text{(E3)}$$

We estimate the bulk temperature using (i) PIC simulations of hot-electron dynamics, (ii) a global energy-budget estimate, and (iii) forward hydrodynamic/PCI modeling.

(i) *PIC estimate.* Using an Al wire as an example, we fit the electron velocity distribution to a Maxwellian[32] at $t = 80$ fs after the laser peak reaches the surface to obtain the bulk thermodynamic temperature [Fig. 9(a)]. The one-dimensional profile at $y = 26$ μm is shown in Fig. 9(b). An exponential envelope $T(x) = Te^{-x/L_s}$ extrapolates the decay to larger distances, yielding $L_s = 5$ μm; thus, along the laser-propagation direction, the bulk temperature at $x = 30$ μm is ~5 eV. Transversely, the hot-electron beam diverges [Fig. 9(a)], the associated return current is much weaker, and the bulk temperature at $z = 30$ μm is ≪5 eV.

(ii) *Global energy budget.* From energy conservation, ~1.35 J of laser energy is contained in the main focal spot; ~20% goes into hot electrons, and assuming ~30% of that is deposited resistively in the bulk, a 60 μm long, 25 μm diameter Cu

segment corresponds to an average specific energy of ~307 MJ/kg. The EOS used in Fig. 9(c) maps this to an average bulk temperature of ~13 eV. In practice, most of this energy is concentrated near the focal region [cf. Fig. 9(a)] and at the surface that drives the cylindrical shock, and allocating only ~30% [assuming a hot-spot radius of 6 μm based on Fig. 9(a)] of the Joule heating to the rest of the bulk yields an average bulk temperature ~2 eV outside the focal zone.

(iii) *Forward phase-contrast-imaging (PCI) modeling.* Using the 2023 dataset,[33] PCI forward calculations for the Cu wire [Fig. 9(d)] indicate that the measurements at $z = 30$ μm fall between the $T_0 = 0.1$ and 5 eV curves, with a closer agreement with 0.1 eV.

Taken together, these diagnostics indicate that the bulk remains at most 2 eV at 30 μm away from the laser focus. Using $P_1/P_2 \lesssim 10^{-2}$ appropriate to the strong-shock regime ($P_2 \sim 10^2$ Mbar), Eq. (E3) gives

$$\Delta U_s/U_{s0} \approx \mathscr{O}(1\%).$$

Consistently, Fig. 9(d) shows that the inferred surface temperatures are $T_e \simeq 250$ and 244 eV for $T_0 = 0.1$ and 5 eV, respectively, with the latter disfavored by the global energy budget. We therefore conclude that treating the bulk as effectively cold is justified, and the strong-
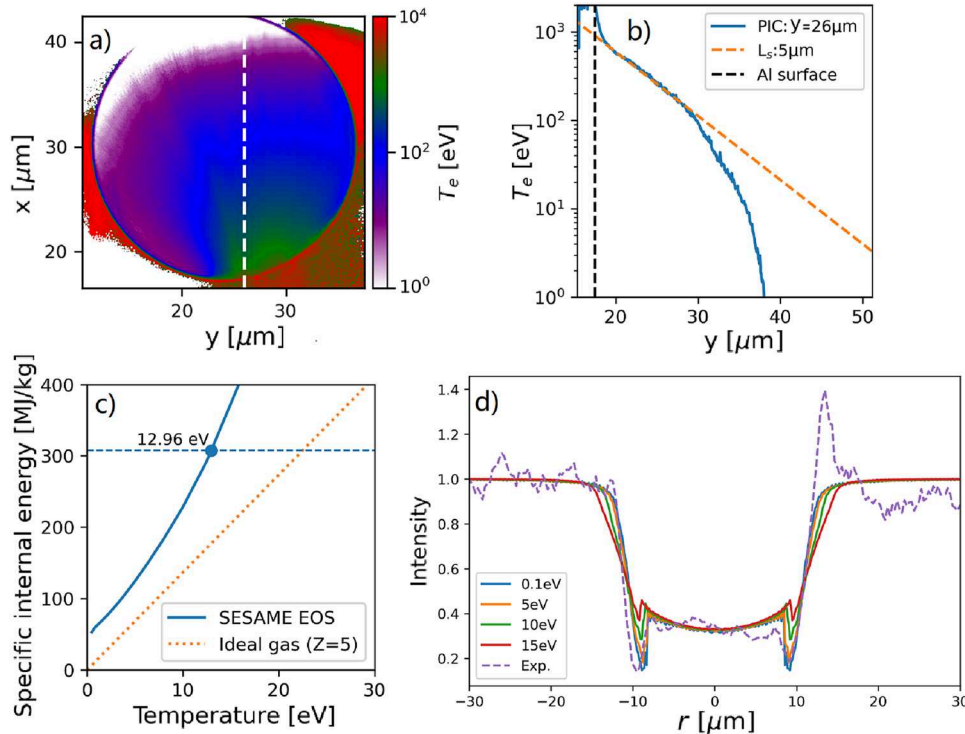

FIG. 9. (a) Two-dimensional maps of the Al bulk electron thermodynamic temperature from PIC simulations at $t = 80$ fs after the laser peak reaches the surface. (b) One-dimensional electron-temperature profile at $y = 26$ μm with an exponential envelope $T(x) = Te^{-x/L_s}$; the black dashed line marks the Al wire surface. (c) Copper specific-internal-energy–temperature relation at 8.93 g/cm^3. (d) Forward PCI calculations using the 2023 dataset[33] for a Cu wire at different initial bulk temperatures T_0, and compared with experiment data measured at 30 μm from the laser focus.
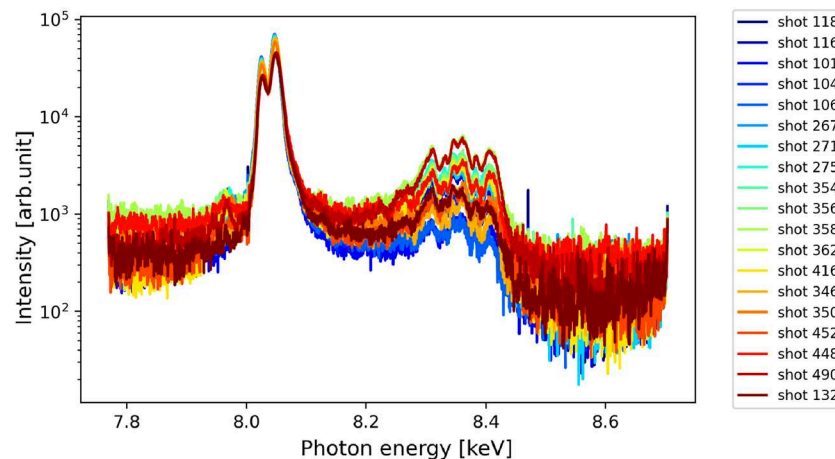
05 February 2026 10:38:38

FIG. 10. Unprocessed X-ray spectroscopy of Cu wires.

shock assumption underlying our surface-return-current inference is self-consistent.

APPENDIX F: Cu K-α SPECTROSCOPY

We present unprocessed X-ray spectra from Cu wires (diameters d = 10–25 μm) in Fig. 10. The counts were recorded directly from the detector, with no background subtraction, no detector-response/flat-field correction, and no absolute photon-number calibration. The XFEL probe beam was on during these measurements. In the Cu K-α region, the spectra show a dominant neutral Cu K-α doublet around 8.05 keV and a weaker complex at 8.33–8.45 keV consistent with He-like/H-like Cu emission. This indicates that the line-of-sight emission is dominated by near-neutral bulk, with only a small hot component, which supports treating the bulk away from the focal region as effectively cold in our analysis. Shots {118, 116, 101, 104, 106, 267, 271, 275} are 25 μm wires, shots {354, 356, 358, 362, 416, 350} are 15 μm wires, and shots {452, 448, 490, 132} are 10 μm wires.

REFERENCES

[1] A. B. Zylstra, O. A. Hurricane, D. A. Callahan, A. L. Kritcher, J. E. Ralph *et al.*, "Burning plasma achieved in inertial fusion," Nature **601**, 542–548 (2022).

[2] C. A. Williams, R. Betti, V. Gopalaswamy, J. P. Knauer, C. J. Forrest *et al.*, "Demonstration of hot-spot fuel gain exceeding unity in direct-drive inertial confinement fusion implosions," Nat. Phys. **20**, 758–764 (2024).

[3] V. Gopalaswamy, C. A. Williams, R. Betti, D. Patel, J. P. Knauer *et al.*, "Demonstration of a hydrodynamically equivalent burning plasma in direct-drive inertial confinement fusion," Nat. Phys. **20**, 751–757 (2024).

[4] R. Betti and O. A. Hurricane, "Inertial-confinement fusion with lasers," Nat. Phys. **12**, 435–448 (2016).

[5] J. D. Lindl, P. Amendt, R. L. Berger, S. G. Glendinning, S. H. Glenzer *et al.*, "The physics basis for ignition using indirect-drive targets on the National Ignition Facility," Phys. Plasmas **11**, 339–491 (2004).

[6] S. H. Glenzer and R. Redmer, "X-ray Thomson scattering in high energy density plasmas," Rev. Mod. Phys. **81**, 1625–1663 (2009).

[7] O. A. Hurricane, D. A. Callahan, D. T. Casey, P. M. Celliers, C. Cerjan *et al.*, "Fuel gain exceeding unity in an inertially confined fusion implosion," Nature **506**, 343–348 (2014).

[8] E. I. Moses, R. N. Boyd, B. A. Remington, C. J. Keane, and R. Al-Ayat, "The National Ignition Facility: Ushering in a new age for high energy density science," Phys. Plasmas **16**, 041006 (2009).

[9] A. Laso Garcia, L. Yang, V. Bouffetier, K. Appel, C. Baehtz *et al.*, "Cylindrical compression of thin wires by irradiation with a joule-class short-pulse laser," Nat. Commun. **15**, 7896 (2024).

[10] L. Yang, M. Rehwald, T. Kluge, A. Laso Garcia, T. Toncian *et al.*, "Dynamic convergent shock compression initiated by return current in high-intensity laser–solid interactions," Matter Radiat. Extremes **9**, 047204 (2024).

[11] P. Ordyna, C. Baehtz, E. Brambrink, M. Bussmann, A. Laso Garcia *et al.*, "Visualizing plasmons and ultrafast kinetic instabilities in laser-driven solids using x-ray scattering," Commun. Phys. **7**, 296 (2024).

[12] T. Kluge, M. Bussmann, H.-K. Chung, C. Gutt, L. G. Huang *et al.*, "Nanoscale femtosecond imaging of transient hot solid density plasmas with elemental and charge state sensitivity using resonant coherent diffraction," Phys. Plasmas **23**, 033103 (2016).

[13] H. Sawada, T. Yabuuchi, N. Higashi, T. Iwasaki, K. Kawasaki *et al.*, "Ultrafast time-resolved 2D imaging of laser-driven fast electron transport in solid density matter using an x-ray free electron laser," Rev. Sci. Instrum. **94**, 033511 (2023).

[14] L. Huang, M. Šmíd, L. Yang, O. Humphries, J. Hagemann *et al.*, "Demonstration of full-scale spatiotemporal diagnostics of solid-density plasmas driven by an ultra-short relativistic laser pulse using an x-ray free-electron laser," Matter Radiat. Extremes **11**, 017201 (2026).

[15] P. Gibbon, "Efficient production of fast electrons from femtosecond laser interaction with solid targets," Phys. Rev. Lett. **73**, 664 (1994).

[16] G. Malka and J. L. Miquel, "Experimental confirmation of ponderomotive-force electrons produced by an ultrarelativistic laser pulse on a solid target," Phys. Rev. Lett. **77**, 75 (1996).

[17] P. Gibbon, *Short Pulse Laser Interactions with Matter: An Introduction* (World Scientific, 2005).

[18] R. A. Snavely, M. H. Key, S. P. Hatchett, T. E. Cowan, M. Roth *et al.*, "Intense high-energy proton beams from petawatt-laser irradiation of solids," Phys. Rev. Lett. **85**, 2945 (2000).

[19] V. Kaymak, A. Pukhov, V. N. Shlyaptsev, and J. J. Rocca, "Nanoscale ultradense z-pinch formation from laser-irradiated nanowire arrays," Phys. Rev. Lett. **117**, 035004 (2016).

[20]F. N. Beg, M. S. Wei, E. L. Clark, A. E. Dangor, R. G. Evans *et al.*, "Return current and proton emission from short pulse laser interactions with wire targets," Phys. Plasmas **11**, 2806–2813 (2004).

[21]A. Hauer and R. J. Mason, "Return-current heating and implosion of cylindrical CO_2-laser-driven targets," Phys. Rev. Lett. **51**, 459 (1983).

[22]R. F. Benjamin, G. H. McCall, and A. W. Ehler, "Measurement of return current in a laser-produced plasma," Phys. Rev. Lett. **42**, 890 (1979).

[23]M. Rehwald, *Laser-Proton Acceleration in the Near-Critical Regime Using Density Tailored Cryogenic Hydrogen Jets* (Technische Universität Dresden, Dresden, 2022).

[24]U. Zastrau, K. Appel, C. Baehtz, O. Baehr, L. Batchelor *et al.*, "The high energy density scientific instrument at the European XFEL," J. Synchrotron Radiat. **28**, 1393–1416 (2021).

[25]T. J. Burgess, "Electrical resistivity model of metals," Technical Report, Sandia National Labs., Albuquerque, NM, 1986.

[26]J. Johnson, "The sesame database," Technical Report, Los Alamos National Lab. (LANL), Los Alamos, NM, 1994.

[27]A. S. Richardson, "2019 NRL plasma formulary," Technical Report, US Naval Research Laboratory, 2019.

[28]S. P. Hatchett, C. G. Brown, T. E. Cowan, E. A. Henry, J. S. Johnson *et al.*, "Electron, photon, and ion beams from the relativistic interaction of petawatt laser pulses with solid targets," Phys. Plasmas **7**, 2076–2082 (2000).

[29]T. E. Cowan, J. Fuchs, H. Ruhl, A. Kemp, P. Audebert *et al.*, "Ultralow emittance, multi-MeV proton beams from a laser virtual-cathode plasma accelerator," Phys. Rev. Lett. **92**, 204801 (2004).

[30]L. G. Huang, M. Molodtsova, A. Ferrari, A. L. Garcia, T. Toncian *et al.*, "Dynamics of hot refluxing electrons in ultra-short relativistic laser foil interactions," Phys. Plasmas **29**, 023102 (2022).

[31]M. Rehwald, S. Assenbaum, C. Bernert, F.-E. Brack, M. Bussmann *et al.*, "Ultrashort pulse laser acceleration of protons to 80 MeV from cryogenic hydrogen jets tailored to near-critical density," Nat. Commun. **14**, 4009 (2023).

[32]L. Yang, L. Huang, S. Assenbaum, T. E. Cowan, I. Goethel *et al.*, "Time-resolved optical shadowgraphy of solid hydrogen jets as a testbed to benchmark particle-in-cell simulations," Commun. Phys. **6**, 368 (2023).

[33]L. Yang, "Return current heating in relativistic laser matter interactions," Ph.D. thesis, Technische Universität Dresden, 2024.

[34]L. Yang, "The propogation of the surface return current along the thin wire generated by high intensity laser solid interactions" (unpublished) (2025).

[35]M. Roth and M. Schollmeier, "Ion acceleration-target normal sheath acceleration," arXiv:1705.10569 (2017).

[36]T. Kluge, T. Cowan, A. Debus, U. Schramm, K. Zeil *et al.*, "Electron temperature scaling in laser interaction with solids," Phys. Rev. Lett. **107**, 205003 (2011).

[37]S. C. Wilks, A. B. Langdon, T. E. Cowan, M. Roth, M. Singh *et al.*, "Energetic proton generation in ultra-intense laser–solid interactions," Phys. Plasmas **8**, 542–549 (2001).

[38]F. N. Beg, A. R. Bell, A. E. Dangor, C. N. Danson, A. P. Fews *et al.*, "A study of picosecond laser–solid interactions up to 10^{19} W cm^{-2}," Phys. Plasmas **4**, 447–457 (1997).

[39]B. Fryxell, K. Olson, P. Ricker, F. X. Timmes, M. Zingale *et al.*, "FLASH: An adaptive mesh hydrodynamics code for modeling astrophysical thermonuclear flashes," Astrophys. J., Suppl. Ser. **131**, 273 (2000).

[40]A. Dubey, K. Antypas, M. K. Ganapathy, L. B. Reid, K. Riley *et al.*, "Extensible component-based architecture for flash, a massively parallel, multiphysics simulation code," Parallel Comput. **35**, 512–522 (2009).

[41]M. Bussmann, H. Burau, T. E. Cowan, A. Debus, A. Huebl *et al.*, "Radiative signatures of the relativistic Kelvin-Helmholtz instability," in *Proceedings of the International Conference on High Performance Computing, Networking, Storage and Analysis, SC '13* (ACM, New York, 2013), pp. 51–512.

[42]C. Bernert, S. Assenbaum, S. Bock, F.-E. Brack, T. E. Cowan *et al.*, "Transient laser-induced breakdown of dielectrics in ultrarelativistic laser-solid interactions," Phys. Rev. Appl. **19**, 014070 (2023).